Motion Compensation for an Unmanned Aerial Vehicle Remote Radar Life Sensor

Robert Nakata, *Member, IEEE*, Brian Haruna, *Member, IEEE*, Takashi Yamaguchi, Victor Lubecke, *Fellow, IEEE*, Shigeru Takayama, *Member, IEEE* and Kiyotsugu Takaba, *Member, IEEE*

***Abstract*—Unmanned Aerial Vehicle (UAV) platforms are ideal for remote life sensing applications including military, humanitarian and post-disaster search and rescue operations. Doppler radar sensors can remotely detect human respiration vital signs to assess triage but any sensor motion will corrupt the signal. The respiration signal can be recovered by measuring the platform motion with a secondary radar and removing the motion induced phase modulation from the primary radar signal that contains both the platform motion and the desired vital signs signal. We simulated and tested a motion compensation algorithm using the dual radar approach and successfully recovered the respiration signal from the radar sensor using a laboratory testbed and on an airborne quadcopter. We measured a signal to motion interference ratio (SIR) improvement of 15 dB to 41 dB on the benchtop motion testbed and an improvement of 26 dB for the radar sensor on an airborne quadcopter.**

Keywords — Algorithms, biomedical sensors, motion compensation, radar subsystem, remote sensing

I. INTRODUCTION

Unmanned Aerial Vehicles (UAVs) have the potential for post-disaster search and rescue missions where triage can be conducted on victims using an on-board radar sensor to detect respiratory motion [1]. Such UAV first responder sensors can sense and communicate a broad range of victim and terrain data for remote assessment by rescuers, as part of a growing range of ubiquitous wireless network tools [2]. Vital signs measurements using a stationary radar sensor have been previously demonstrated [3]-[8].

This research project attempts to compensate for the motion of the radar sensor on the UAV platform through the use of sensor techniques to minimize signal distortion from the UAV motion.

This paper was submitted on Sep 16, 2017. This work was supported in part by the National Science Foundation (NSF) under CBET-1160326, University of Hawaii at Manoa and the NSF/Japan Society for the Promotion of Science (JSPS) East Asia Pacific Summer Institute post-doctoral fellowship hosted at Ritsumeikan University, Japan (EAPSI award number 1714028).

R. Nakata is a PhD graduate of the Department of Electrical Engineering, University of Hawaii at Manoa, Honolulu, HI 96816 and a Visiting Professor at Ritsumeikan University, Shiga, Japan (email: bob.nakata@gmail.com).
B. Haruna is a graduate of the Department of Electrical Engineering, University of Hawaii at Manoa, Honolulu, HI 96816 (email: bharuna@hawaii.edu)
V.M. Lubecke, PhD is a Professor at the Department of Electrical Engineering, University of Hawaii at Manoa, Honolulu, HI 96816 (email: lubecke@hawaii.edu)
T . Yamaguchi is a graduate student at Ritsumeikan University, Shiga, Japan (email: re0065pi@ed.ritsumei.ac.jp)
S. Takayama, PhD is a Professor at Ritsumeikan University, Shiga, Japan (email: s-tkym@se.ritsumei.ac.jp)
K. Takaba, PhD is a Professor at Ritsumeikan University, Shiga, Japan (E-mail: ktakaba@fc.ritsumei.ac.jp)

Other papers describe motion cancellation techniques for vital signs sensing when the subject motion interferes with the measurement [9], [10]. For a Doppler radar system, the radar return signal corresponds to the phase modulation resulting from the range variation between the radar and the subject and any sensor platform motion will induce an undesired phase component to the baseband signal. For our concept of operations, the assumption is that the human subject is stationary, as is likely the case for a post-disaster scenario where victims are prone on the ground and the primary component of signal distortion is from the UAV motion. Prior work focused on the characterization of the Received Signal Strength Indicator (RSSI) and RF Direction of Arrival (DOA) of commercially available radar modules to stabilize the airborne platform [11], [12].

In this paper, we report on the investigation results of the application of (1) physical *platform stabilization* using ultrasonic and camera sensors for motion compensation and (2) compensating for the platform motion using a signal processing *motion compensation* algorithm. Physical platform stabilization uses an ultrasonic sensor Proportional Integral Derivative (PID) feedback loop to maintain a nearly constant range between the radar sensor and the target to reduce the overall platform motion to a manageable range for the motion compensation signal processing algorithm to be effective. Any residual phase modulation due to the remaining platform motion is reduced by applying a compensating phase term to the composite signal in the motion compensation algorithm. The composite signal is measured by the primary radar whose phase is modulated by the platform motion and the target respiratory motion. The platform motion is measured by a second radar that is pointed at the ground at an offset angle. The offset angle ensures that the platform radar phase is proportional to the platform motion only and does not include the target in the field of view.

We measured the physical stabilization performance using an ultrasound and radar PID feedback loop on a bench top testbed. We induced signal distortions emulating the motion of a hovering drone by mounting the testbed on a programmable linear actuator. We then measured the effect of the PID feedback loop on the reduction of physical motion by driving a second actuator mounted on the base actuator. Since the PID loop does not completely cancel the platform motion, any remaining phase distortion is removed with the motion compensation signal processing algorithm.

In addition to the lab tests, we mounted the radars on a ARDrone 2.0 quadcopter with a built-in camera and ultrasonic sensor and analyzed the motion compensation performance.

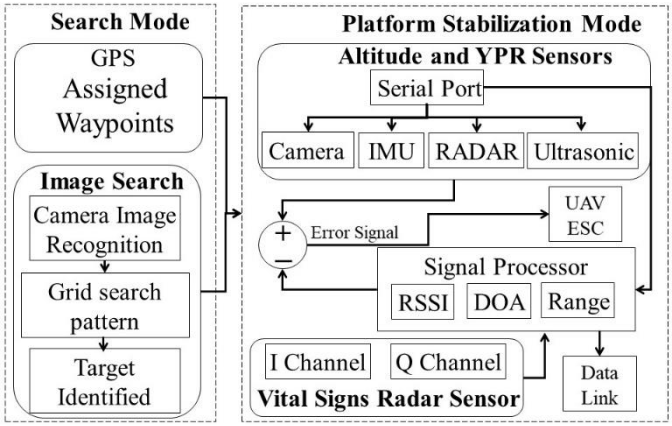

Fig. 1. Operational mode diagram for the search and stabilization modes for the UAV radar sensor platform. Conventional sensors (GPS, IMU and ultrasonic sensors) that determine altitude and yaw, pitch, roll (YPR) are supplemented with radar and image sensors to provide inputs for vertical and lateral stabilization.

Hover and loiter modes of existing drones that rely on GPS or barometric and ultrasonic sensors to maintain a stationary altitude are prone to vertical and horizontal drift and are not sufficiently stable enough to serve as platforms for radar life sensing. We show that real-time lateral motion compensation using an onboard camera to generate an error signal for a closed loop feedback system can be used to adjust the on-board Electronic Speed Controllers (ESC) that control the propeller speed for each quad-copter motor, thereby stabilizing the platform. Yaw, Pitch and Roll (YPR) commands are used to stabilize the platform while hovering over the respiration mover target.

The operational concept is for the system to have a search mode and an acquisition mode as shown in Fig 1. In the search mode, the UAV navigates to the area of interest using GPS waypoint coordinates. At the waypoint station, an onboard camera with image recognition identifies potential victims (targets). In the stabilization mode, sensor fusion of secondary sensors, including GPS, IMU, radar and/or ultrasonic range sensors, are used to adjust the UAV ESCs to maintain a steady altitude and fixed Yaw, Pitch and Roll (YPR) attitude. In the target acquisition mode, the UAV autonomously converges above the subject and uses the camera and ultrasonic sensor to maintain a steady hover position over the target.

We modified an ARDrone 2.0 quad-copter by adding an instrumentation payload, communications, data logging and real-time flight control subsystem and collected and analyzed the radar data. The platform block diagram is shown in Fig 2.

II. QUADRATURE RADAR BACKGROUND

The radar equation describes the signal transmission and reception when the transmitted waveform is reflected from a target object with a given Radar Cross Section (RCS).
Doppler radar measures target motion via the return signal phase. The Doppler effect and range to target are described by

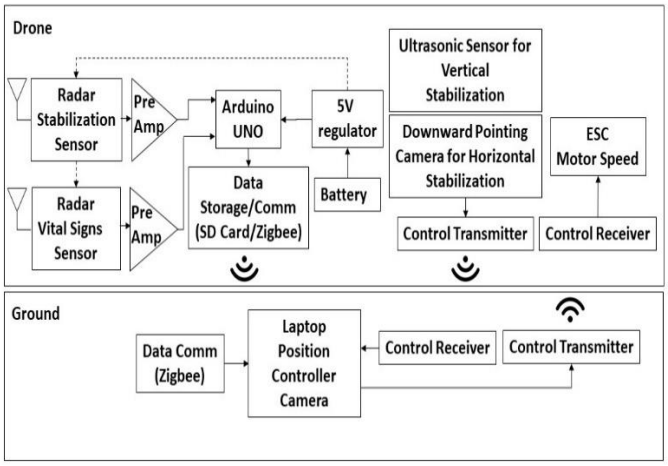

Fig. 2. System block diagram showing radar payload, signal conditioning, data downlink and ground-based baseband signal processor.

$$\Delta f = \frac{2f \cdot v(t)}{\mathrm{c}} = \frac{2 \cdot v(t)}{\lambda} \tag{1}$$

and

$$R = \frac{\mathrm{c} \cdot T}{2} \tag{2}$$

where Δf is the receiver frequency shift, f is the transmitter frequency, $v(t)$ is the target velocity, c is the speed of light, λ is the RF wavelength and T is the measured transit time between transmission and reception.

The radar transmits the waveform

$$T(t) = \cos\left(2\pi f_t t + \varphi(t)\right) \tag{3}$$

and the received waveform is

$$R(t) = A\cos\left(2\pi f_t t + p(t) + \theta + \varphi\left(t - \frac{2R}{\mathrm{c}}\right)\right) \tag{4}$$

where A is the amplitude, f_t is the transmitter frequency, $\varphi(t)$ is the transmitter phase offset, θ is the fixed phase offset inherent in the receiver hardware, $p(t)$ is the phase modulation from the respiration motion and $\varphi\left(t - \frac{2R}{\mathrm{c}}\right)$ is the phase delay due to the roundtrip signal propagation. Since this is a CW Doppler radar, we are interested in the measuring the phase change in the backscattered signal from the target.

A coherent receiver down converts the received signal by mixing the received signal with a quadrature mixer. The quadrature mixer uses a phase shifter to generate a quadrature component that is shifted by 90 degrees. This allows the received signal to be deconstructed into two components that are 90 degrees apart, thus ensuring that when the in-phase (I) component is at a null, the quadrature component is at a peak. Quadrature (Q) decomposition also mathematically allows any complex signal to be represented by its orthogonal components with appropriate amplitude and phase scaling. See Fig. 3.

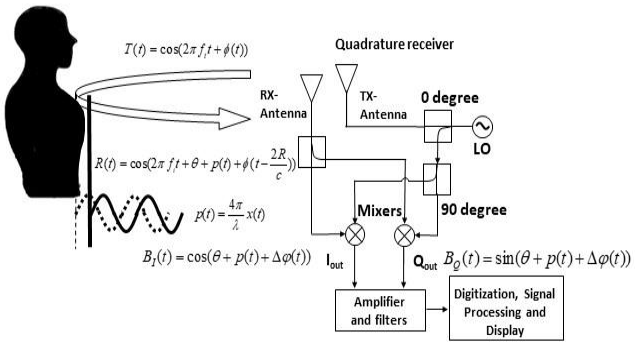

Fig. 3. Quadrature radar transceiver block diagram to detect respiration motion.

Since the received signal is multiplied by the same Local Oscillator (LO) as the transmitter LO, the transmitted and received signals are said to be coherent. Multiplying the received signal by the LO down converts the RF signal to baseband. Since the receiver LO is a replica of the transmitter LO, any phase noise or frequency drift is also removed in the down conversion process.

The two receiver channels are referred to as an in-phase (I) channel and quadrature phase (Q) channel. The I and Q channels are represented as

$$B_I(t) = \cos\big(\theta + p(t) + \Delta\varphi(t)\big) \tag{5}$$

$$B_Q(t) = \sin(\theta + p(t) + \Delta\varphi(t)) \tag{6}$$

where $p(t)$ is the phase modulated signal of interest that is corrupted by the platform motion that manifests as a phase term, $\Delta\varphi(t)$.

Note that the chest displacement $x(t)$ will contribute to the magnitude of the phase modulation of the reflected signal. Thus the Signal to Noise Ratio (SNR) will vary with the magnitude of the respiration motion with the overall SNR determined by the antenna gain, transmitter power, receiver gain, receiver noise figure, range and background clutter.

Let the physiological motion of the thorax expanding and contracting be defined as $x(t)$.The resulting phase modulation component from the variable range to the thorax detected by the radar is

$$p(t) = \frac{4\pi}{\lambda} x(t) \tag{7}$$

The average respiration motion is 4 to 12 mm and the average adult respiration rate is 12 to 15 Breaths per Minute (BPM) [13]. Detecting the respiration signal $p(t)$ in the presence of platform motion requires suppression of the $\Delta\varphi(t)$ term. The remaining sections of this paper describe techniques to recover the signal using sensor fusion to stabilize the platform and signal processing to compensate for the platform motion.

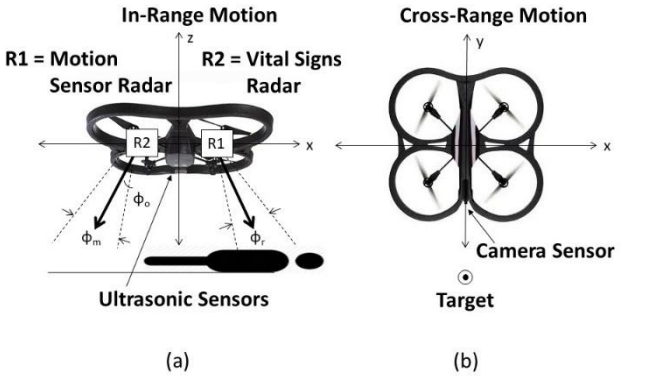

Fig. 4. Quadcopter radar remote sensing platform sensor geometry. (a) Primary radar R1 measures respiration and platform motion while the secondary radar R2 sensor measures platform motion for motion compensation. Vertical platform stabilization uses the ultrasonic sensor. (b) Camera feedback loop that locks on to a fixed target provides lateral platform stabilization.

Figure 4 illustrates the sensor pointing geometry for the primary and secondary sensors. The primary radar sensor detects the signal of interest while the secondary sensor measures the platform motion with respect to the ground or ceiling, if indoors. Care must be exercised such that $\varphi_m/2 < \varphi_o$ and $\varphi_r/2 < \varphi_o$ to avoid range motion sensor and vital sign sensor overlap, where φ_m is the motion sensor radar beamwidth, φ_r is the respiration sensor radar beamwidth and φ_o is the outward slant angle from the vertical for each radar boresight. The 10 GHz radar module has a half power beamwidth (HPBW) of 36 degrees so each module was slanted outward by 20 degrees from the vertical.

III. MOTION COMPENSATION ALGORITHM

The time domain representations for the vital sign signal of interest (modeled as a sinusoid for simplicity but applicable to complex signals because of superposition) and platform motion components are the respiration signal

$$R_1(t) = A\sin(\omega_1 t) \tag{8}$$

and the platform motion signal

$$R_2(t) = B\sin(\omega_2 t) \tag{9}$$

where $\omega_1 = 2\pi f_1$ and $\omega_2 = 2\pi f_2$ are the angular frequencies for the respiration signal to be recovered and the undesirable platform motion, respectively. Substituting (7), (8) and (9) into (5), the in-phase respiration baseband radar signal is

$$S_{Resp}(t) = \cos\left(\frac{4\pi A}{\lambda}\sin(\omega_1 t)\right) \tag{10}$$

and the in-phase platform motion radar signal is

$$S_{Plat}(t) = \cos\left(\frac{4\pi B}{\lambda}\sin(\omega_2 t)\right). \tag{11}$$

The composite waveform is the combined platform motion and respiration motion. This is the baseband signal output from the respiration radar as a result of the superimposed platform motion and respiration motion.

The combined composite motion detected by the primary radar sensor is

$$S_{Composite}(t) = \cos(4\pi A/\lambda \ \sin(\omega_1 t) + 4\pi B/\lambda \ \sin(\omega_2 t)\ ). \quad (12)$$

Using the cosine angle sum identity:

$$\cos(a+b) = \cos a \cos b - \sin a \sin b \quad (13)$$

the composite motion detected by the primary radar is

$$S_{Composite}(t) = \cos\left(\frac{4\pi A}{\lambda}\sin(\omega_1 t) + \frac{4\pi B}{\lambda}\sin(\omega_2 t)\right)$$
$$= \cos\left(\tfrac{4\pi A}{\lambda}\sin(\omega_1 t)\right)\cos\left(\tfrac{4\pi B}{\lambda}\sin(\omega_2 t)\right) - \sin\left(\tfrac{4\pi A}{\lambda}\sin(\omega_1 t)\right)\sin\left(\tfrac{4\pi B}{\lambda}\sin(\omega_2 t)\right) \quad (14)$$

The compensated waveform $S_{compensated}(t)$ is derived from removing the phase modulation induced by the undesired platform motion within the composite phase terms.

$$S_{compensated}(t) = \cos\left(\tfrac{4\pi}{\lambda}[A\sin(\omega_1 t) + B\sin(\omega_2 t)] - \tfrac{4\pi}{\lambda}\mathrm{B}\sin(\omega_2 t)\right) \quad (15)$$

where the terms in the brackets represent the composite waveform measured by the primary radar. Therefore, the second ω_2 sinusoid term cannot be merely subtracted from the first ω_2 sinusoid term in the cosine expression when processing the actual radar signal outputs.

Using the cosine angle difference identity,

$$\cos(a-b) = \cos a \cos b + \sin a \sin b \quad (16)$$

$$S_{compensated}(t) = \cos\left(\tfrac{4\pi}{\lambda}(A\sin(\omega_1 t)\, B\sin(\omega_2 t))\right)\cos\left(\tfrac{4\pi}{\lambda}B\sin(\omega_2 t)\right) + \sin\left(\tfrac{4\pi}{\lambda}(A\sin(\omega_1 t) + \mathrm{B}\sin(\omega_2 t))\right)\sin\left(\tfrac{4\pi}{\lambda}\mathrm{B}\sin(\omega_2 t)\right) \quad (17)$$

As an alternative, the motion compensation phase can be analyzed in the complex IQ (In-phase and Quadrature) domain as depicted in Figure 5. The primary vital signs radar detects the composite motion while the secondary radar detects the platform motion with respect to the ground (or ceiling if indoors). By removing the platform motion phasor rotation from the composite motion phasor, the remaining phasor rotation is due to the respiration motion. The arc length corresponds to the amount of motion. A phenomenon referred to as phase wrapping occurs when the motion exceeds a half wavelength.

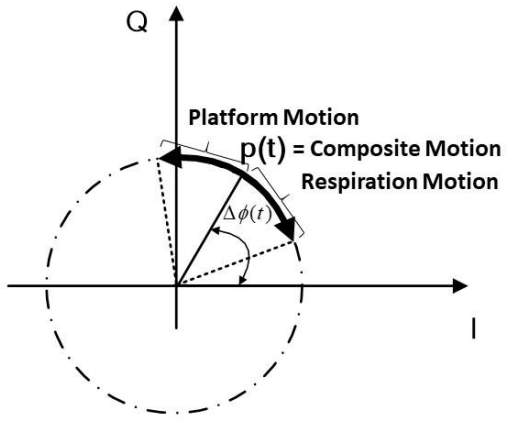

Fig. 5. Phasor representation of the respiration motion, platform motion and combined motion.

The complex representations for each component are:
Respiration motion:

$$R_{respiration} = A \cdot \mathrm{Re}\left[\mathrm{e}^{-\mathrm{j}2\pi f_{respiration} t}\right] \quad (18)$$

Platform motion:

$$S_{platform} = B \cdot \mathrm{Re}\left[\mathrm{e}^{-\mathrm{j}2\pi f_{platform} t}\right] \quad (19)$$

Composite motion:

$$S_{composite} = A \cdot B \cdot \mathrm{Re}\left[\mathrm{e}^{-\mathrm{j}\frac{4\pi}{\lambda}(R_{respiration}+R_{platform})}\right] \quad (20)$$

Subtracting the platform component from the composite motion results in

$$S_{compensated} = A \cdot B \cdot \mathrm{Re}\left[\mathrm{e}^{-\mathrm{j}\frac{4\pi}{\lambda}(R_{composite}-R_{platform})}\right] \quad (21)$$

where $R_{composite}$ is the output for the radar sensor pointed at the respiration phantom that sees both the phantom and the platform motion and $R_{platform}$ is the radar sensor output pointed at the ground. The motion compensated signal, $S_{compensated}$, is the desired respiration motion recovered from the composite motion seen by the respiration radar sensor. This equation was implemented in MatLab to simulate the algorithm as described next in Section IV. Equation (21) was also used in MatLab to process the two radar sensor outputs from the quadcopter.

IV. Motion Compensation Simulation

A MATLAB simulation program was written to simulate the effect of the UAV platform motion on the respiration signal of interest. The plots in Figure 6 show the simulated platform motion and respiration motion and the composite and compensated waveforms.

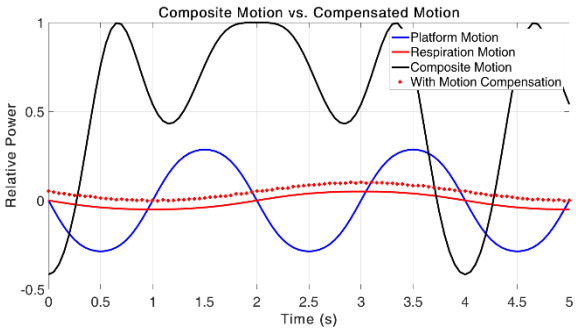

Fig. 6. Time domain simulation of the platform and respiration baseband radar waveforms for 17 mm platform amplitude at 0.5 Hz and 3mm respiration amplitude at 0.25 Hz. Recovered waveform with motion compensation is offset for clarity.

When the amplitude of the platform motion exceeds one half of the radar wavelength, a phenomenon known as phase wrap occurs. When this occurs, additional peaks are introduced in the time domain, creating harmonics in the frequency domain. Platform stabilization is used to reduce the likelihood of phase wrapping so that the motion compensation algorithm can be effective.

V. TESTBED EXPERIMENT CONFIGURATION

The motion compensation experiment block diagram is shown in Figure 7. The target signal of interest is created with the Mover 1 linear actuator representing respiration motion. The UAV platform motion is created with Mover 3 using a programmable linear actuator from Galil Motion Systems. The Mover 2 was implemented using a slide potentiometer linear actuator mounted on wheels to allow independent motion from the Mover 3 base platform. An Arduino UNO controller was programmed to control the position of Mover 2 in real time based on the ultrasonic sensor or secondary range value. If optimally implemented, Mover 2 will cancel the undesirable Mover 3 motion. The test platform hardware configuration is shown in Figure 8.

For the physical platform motion control to be effective, the compensation counter-motion must meet the following conditions: (1) the corrective motion latency should be near zero (2) the magnitude of the corrective motion should be equal to the disturbance magnitude (3) the speed of the corrective motion should be identical to the disturbance speed. Although these ideal conditions were difficult to achieve, tuning the (PID) feedback loop parameters in multiple iterations resulted in sufficient reduction of the platform motion such that the residual motion could be compensated with the phase domain signal processing described earlier.

The primary and secondary radars used were Commercial-off-the-shelf (COTS) MDU1100T 10.5 GHz radar modules from Microwave Solutions. The transmitter has a 10dBm Effective Isotropic Radiated Power (EIRP) and the antenna beam has a H-plane Half Power Beamwidth (HPBW) of 36 degrees. The radar receiver has a -86 dBm sensitivity at 10 dB SNR. DC power consumption is 40mA with a 5V power supply.

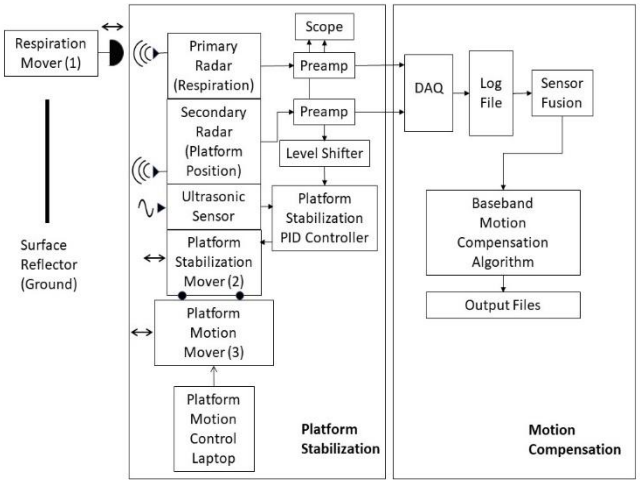

Fig. 7. Platform stabilization and motion compensation experiment block diagram. The respiration signal of interest (Mover 1) is detected by the primary radar that is mounted on the motion compensator (Mover 2) that is mounted on the base platform representing the unwanted motion from a UAV (Mover 3). Mover 2 is driven by either an ultrasonic sensor or a secondary radar sensor that detects the platform motion relative to a stationary reflector representing the ground.

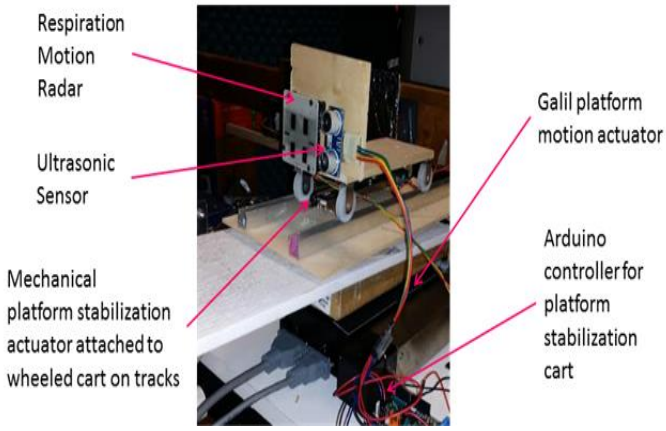

Fig. 8. Platform stabilization cart with ultrasonic sensor and primary radar sensor mounted on moving platform.

The primary radar output signal was amplified by a pre-amp with a passband from 0.3 Hz to 10 Hz and a gain of 20 dB. The preamp output was digitized by a National Instruments data acquisition (DAQ) system set at a 1 KHz sampling rate. The DAQ was configured with a LabView Graphical User Interface (GUI) and the data log files were saved as text files that were post-processed in MATLAB.

The ultrasonic sensor was a COTS HCSR04 with a 30 degree beamwidth, 4 meter range and 0.3 cm resolution. For the platform stabilization PID feedback control loop, an Arduino Uno was used, with software tuning of the proportional gain, integral and derivative parameters. Both the radar and ultrasonic sensors were tested with the PID loop.

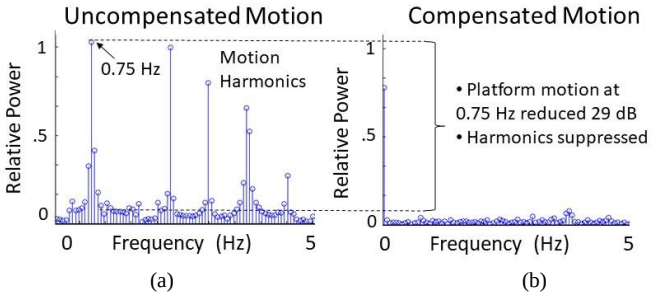

Fig. 9. Motion compensation algorithm effectiveness. (a) Radar signal spectrum with uncompensated platform motion at 0.75 Hz and 22mm displacement (b) Spectrum after motion compensation.

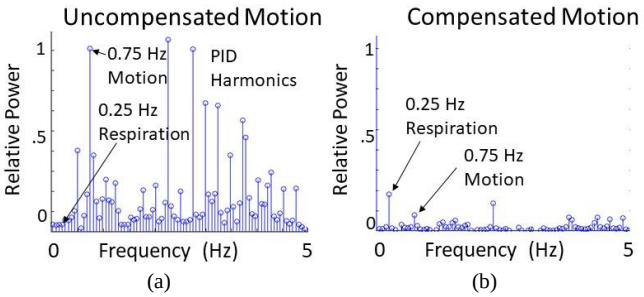

Fig. 10. Benchtop testbed platform motion with 23 mm displacement at 0.75 Hz and respiration motion with 3 mm displacement at 0.25 Hz. (a) spectrum without motion compensation (b) spectrum after secondary radar motion compensation with 33.5 dB SIR improvement. Harmonics are introduced by ultrasonic sensor platform stabilization PID loop jitter and reduced by the motion compensation algorithm.

VI. TESTBED EXPERIMENTAL RESULTS

Experiments were performed using the laboratory testbed to test the effectiveness of the platform stabilization and motion compensation algorithm by comparing the Signal to Interference Ratio (SIR) before and after the baseband motion compensation.

Since the Signal to Noise (SNR) is a function of the receiver Noise Figure (NF) and the resulting noise equivalent bandwidth is determined by the receiver passband that varies by receiver design, a convenient metric is to compare the SIR. Factors such as the receiver noise equivalent bandwidth and thermal noise are not relevant to the motion compensation gain and therefore the SIR is an appropriate benchmark to assess the motion compensation performance improvement. The SIR is defined by

$$\mathrm{SIR} = 20\log\left(\frac{V_{resp}}{V_{plat}}\right) \tag{22}$$

where V_{resp} is the voltage magnitude of the respiration signal and V_{plat} is the voltage magnitude of the platform signal in the frequency domain.

The effectiveness of the motion compensation algorithm in removing the platform motion is shown in Fig 9. If the platform motion is perfectly canceled, the compensated waveform should be a constant value. The harmonics are a result of mechanical jitter introduced by the ultrasonic sensor PID controller in the Mover 3 feedback loop. Additional harmonic content is introduced by the phase wraparound and is also suppressed by the motion compensation signal processing. The spectrum for the combined platform motion and respiration motion with and without the motion compensation algorithm is shown in Fig. 10.

To isolate the motion compensation algorithm performance, experiments were conducted *without* stabilizing the platform motion where the PID loop was disabled. Table 1 summarizes the motion compensation algorithm performance in reducing the magnitude of the platform motion. The amount of motion reduction diminishes with an increase in platform motion beyond the radar wavelength (30 mm at 10 GHz), as expected, due to the phase wrapping.

The motion compensation algorithm is very effective in improving the SIR with a range of improvement from 6 dB to 42 dB for 16 test cases with the mean SIR improvement of 19 dB. Without motion compensation enabled, the same test cases had SIR values between -29 dB to 6 dB with the mean SIR = -5.5 dB.

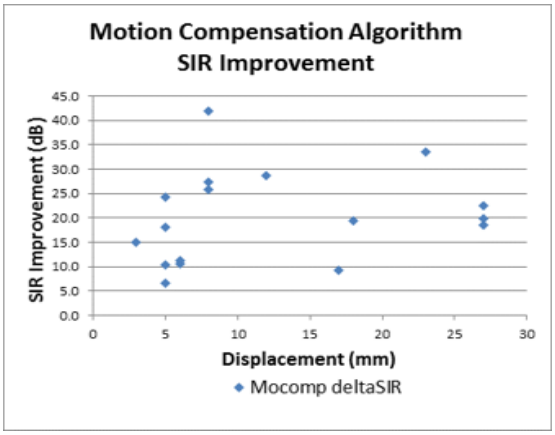

Fig. 11. Motion compensation algorithm SIR improvement with mean = 19 dB and standard deviation = 10.3 dB for various platform motion displacements.

TABLE 1
MOTION COMPENSATION ALGORITHM PERFORMANCE

Platform Displacement	Signal to Interference Ratio (dB) Improvement
6 mm	41.9
12 mm	35.0
18 mm	40.9
22 mm	41.5
38 mm	15.8

Motion compensation algorithm Signal to Interference Ratio (SIR) improvement with sinusoidal platform motion at 0.75 Hz. Platform stabilization PID feedback loop was disabled to assess motion compensation algorithm performance.

The SIR scatter plot and SIR improvement are summarized in Fig. 11. All SIR improvement values in the scatter plot are with respect to the baseline measurements before motion compensation was applied. The scatter plot is a compilation of the SIR improvement for various respiration motion frequencies from 0.25 Hz to 1.25 Hz and respiration motion magnitudes ranging from 5 mm to 10 mm. The motion

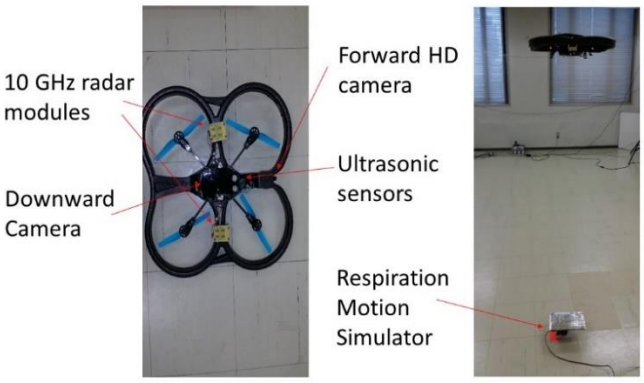

(a) (b)

Fig. 12. ARDrone 2.0 with radar modules, built-in cameras and ultrasonic sensors. A respiration motion simulator was used to collect the radar data while in flight.

compensation algorithm improved the SIR with a mean improvement of 19 dB and standard deviation of 10.3 dB. The mean improvement of 19 dB shows the effectiveness of the algorithm.

VII. Quadcopter Radar Experimental Results

For the flight experiments, the author collaborated with researchers at Ritsumeikan University in Japan who have developed an autonomous navigation system for the ARDrone 2.0. The quadcopter was outfitted with two Microwave Solutions MDU1100T 10.5 GHz radar modules, preamplifiers assembled from LM324 op amps and filters for data conditioning, and an Atmel ATMega328 processor to digitize the data and provide a serial output. The serial output was transmitted over a Zigbee link and also written to and stored on an on-board SD card for subsequent analysis. See Fig. 2 and Fig. 12(a). All components were powered by a LM7805 5 volt regulator that was used to regulate the voltage from a supplemental LiPo battery pack.

Since the HPBW of the radar modules is 36 degrees, the radar modules were mounted to the ARDrone structure pointing outboard by approximately 20 degrees from the vertical to avoid antenna beam overlap as described earlier in Section II.

The ARDrone has built-in ultrasonic sensors that provide altimeter data and are used to adjust the vertical thrust to maintain a constant altitude in the vertical direction. The front camera imagery is used to maintain a constant position in the horizontal plane by tracking a fixed target. Real-time quadcopter flight control software was used to maintain a fixed altitude and horizontal position. Some residual lateral motion of 10 mm to 15 mm remains and the altitude is maintained within +/- 2 cm using the ultrasonic altimeter feedback loop. The built-in camera tracks an illuminated light bulb that serves as a position marker. Any lateral drift is corrected and as a result the quadcopter maintains a steady horizontal position. For future versions, image processing with object recognition can use any ground based object as a marker.

The control loop uses Linear Quadratic Integral (LQI) parameters that include the quadcopter mass, moment of inertia, center of gravity and torque that are obtained empirically using system identification techniques. Because there are delays introduced by the WiFi communications link and image capture, the control loop uses state augmentation to handle the time delays [14]-[17].

The quadcopter was flown approximately 1 meter above a respiration phantom target programmed to move at slightly greater than 6 breaths per minute or 0.14 Hz. See Fig. 12(b). The target RCS was calculated as 1.3 m^2 or 2.6 dBsm for a flat plate at 10.5 GHz, which is consistent with human torso RCS reported in the literature [18].

An example power spectrum collected on the quadcopter for the radar signal with and without the motion compensation algorithm is shown in Fig. 13. The respiration signal is masked by the motion noise and recovered with the motion compensation signal processing. The SIR improvement is 26 dB although the actual improvement will be greater depending on the receiver passband given the wideband noise content. Fig. 14 shows the uncompensated and compensated power spectrum without the respiration phantom in the radar field of view, confirming that the peak in Fig 13 is the respiration signal. The uncompensated composite, motion compensated and idealized respiration time domain signals are shown in Fig. 15.

In the presence of background clutter, as long as the magnitude of the signal of interest (SOI) is greater than the magnitude of the ground clutter Doppler spread, we expect to recover the SOI. Several techniques can be used to reduce the DC offset resulting from the clutter, including the center estimation algorithm [19]. We can also reduce the effect of the clutter by using the coarse-tuning technique at the RF front end [20] and remove the remaining DC offset by using the baseband fine-tuning approach [21].

VIII. CONCLUSIONS

We conclude that a radar sensor mounted on a stabilized airborne quadcopter can detect the respiration motion of a stationary target on the ground. Although a servo driven respiration motion simulator was used, the radar cross section, displacement and frequency of the simulator is similar to that of human respiratory motion and served as an adequate proxy.

Real-time physical platform stabilization is required to reduce the motion to less than one-half the radar wavelength, so that phase wrapping is avoided and the motion compensation algorithm is effective. In our case, we used the built-in ultrasonic sensor on the quadcopter that provided an error signal for the real-time altitude stabilization feedback loop. Horizontal drift was minimized using a real-time image tracking feedback loop.

Once the platform is stabilized, any remaining residual motion can be compensated for using a phase compensation algorithm that uses a secondary radar to measure the vertical displacement. Using this approach, we observed an average 26 dB SIR improvement for the airborne quadcopter sensor, where the signal is the respiration mover motion as detected by the radar and the interference is the primary frequency component of the platform motion as detected by the radar.

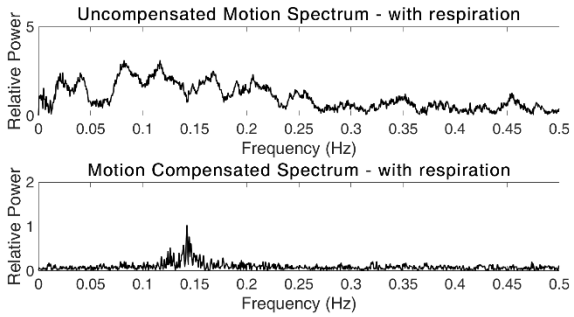

Fig. 13. Radar data collected from platform stabilized hovering drone using ultrasonic sensor for altitude stabilization and camera sensor for lateral stabilization. Radar signal spectrum with the respiration phantom in radar field of view before (top) and after (bottom) applying the motion compensation algorithm showing the recovered respiration signal.

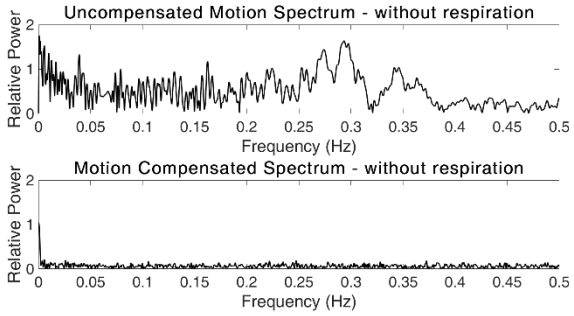

Fig. 14. Radar data collected from the platform stabilized hovering drone using ultrasonic and camera sensors without the respiration phantom in the radar field of view. Uncompensated (top) and compensated (bottom) shows the effectiveness of the motion compensation algorithm in reducing the motion noise.

ACKNOWLEDGMENT

This work was supported in part by the National Science Foundation (NSF) under CBET-1160326, University of Hawaii at Manoa and the NSF/Japan Society for the Promotion of Science (JSPS) East Asia Pacific Summer Institute post-doctoral fellowship hosted at Ritsumeikan University, Japan (EAPSI award number 1714028).

REFERENCES

[1] V. Ferrara, "Technical Survey About Available Technologies For Detecting Buried People Under Rubble Or Avalanches," *WIT Transactions on The Built Environment*, vol 150, pp. 91-101, May 2015.

[2] Debabani Choudhury, "5G wireless and millimeter wave technology evolution: An overview," 2015 IEEE MTT-S International Microwave Symposium, pp. 1 – 4, 2015

[3] V. Lubecke, O. Boric-Lubecke, J. Lin, C. Li, "A review on recent advances in Doppler radar sensors for noncontact healthcare monitoring," IEEE Trans. Microwave Theory and Techniques, vol. 61, no. 5, pp. 2046-2060, May 2013.

[4] A.D. Droitcour, O. Boric-Lubecke, V.M. Lubecke, J. Lin and G.T.A. Kovac, "Range correlation and I/Q performance benefits in single-chip silicon Doppler radars for noncontact cardiopulmonary monitoring," IEEE Trans. Microw. Theory Tech., vol. 52, no.3, pp. 838-848, Mar. 2004.

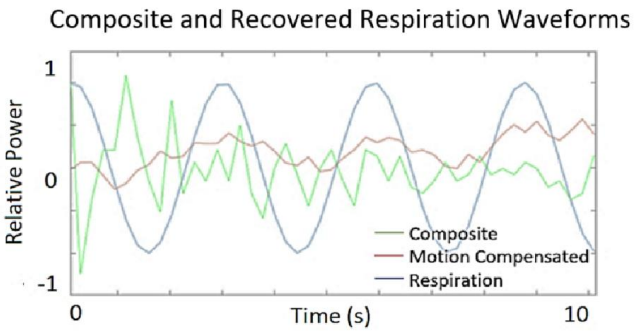

Fig. 15. Time domain signal of the primary radar output before and after motion compensation. Green plot is the uncompensated primary radar signal with the composite respiration and platform motion signal and the red plot is the recovered respiration signal after applying the motion compensation algorithm. For reference, the ideal 0.14 Hz respiration waveform is superimposed in blue.

[5] Jenshan Lin, "Noncontact measurement of cardiopulmonary movements: A review of system architectures and the path to micro-radars," 2013 IEEE MTT-S International Microwave Workshop Series on RF and Wireless Technologies for Biomedical and Healthcare Applications (IMWS-BIO), pp. 1 – 3, 2013.

[6] Takuya Sakamoto, Ryohei Imasaka, Hirofumi Taki, Toru Sato, Mototaka Yoshioka, Kenichi Inoue, Takeshi Fukuda, and Hiroyuki Sakai, "Accurate heartbeat monitoring using ultra-wideband radar," IEICE Electronics, Express, vol. 12, no. 3, pp.20141197, 2015.

[7] Leem, Seong Kyu, Faheem Khan, and Sung Ho Cho. "Vital Sign Monitoring and Mobile Phone Usage Detection Using IR-UWB Radar for Intended Use in Car Crash Prevention." Sensors 17, no. 6 (2017): 1240.

[8] Z. Peng, J.-M. Muñoz-Ferreras, Y. Tang, R. Gómez-García, L. Ran, and C. Li, "A portable FMCW-interferometry radar with programmable low-IF architecture for localization, ISAR imaging and vital-sign tracking," IEEE Transactions on Microwave Theory and Techniques, vol. 65, no. 4, pp. 1334-1344, Apr. 2017.

[9] C. Li and J. Lin, "Random Body Movement Cancellation in Doppler Radar Vital Sign Detection," *IEEE Trans. on Microw. Theory Techn.*, vol. 56, no. 12, pp. 3143-3152, Nov. 2008.

[10] I. Mostafanezhad, V. Lubecke, O. Boric-Lubecke, "Application of empirical mode decomposition in removing fidgeting interference in Doppler radar life signs monitoring devices," in IEEE Int. Eng. Med. Biol. Soc. Conf, Minneapolis.

[11] R. Nakata, S. Clemens, A. Lee, V. Lubecke, "RF Techniques for Motion Compensation of an Unmanned Aerial Vehicle for Remote Radar Life Sensing," IMS 2016 conference paper, San Francisco, CA, May 2016.

[12] R. Nakata, B. Haruna, S. Clemens, D. Martin, C. Jaquiro, V. Lubecke, "Unmanned Aerial Vehicle Platform Stabilization for Remote Radar Life Sensing," Applied Computational Electromagnetics Society Express Journal, Special Issue, August, 2016

[13] O. Boric-Lubecke and et. al., Doppler Radar Physiological Sensing, Wiley, 2015.

[14] K. N. Y. Takaba, "Visual Feedback Altitude Control of Quadcopters," in Proceedings of the 50th Annual Conference of the Institute of Sytems, Control and Information Engineers (ISCIE), Osaka, May 20-22, 2015.

[15] T. Fujinaka and M. Araki: "Discrete-time optimal control of systems with unilateral time-delays," Automatica,vol. 23, no. 6, pp. 763-765, 1987.

[16] F. Liao, K. Takaba, and T. Katayama: "Design of an optimal preview servomechanism for discrete-time systems in a multirate setting," Dynamics of Continuous, Discrete and Impulsive Systems: Series B, vol.10, pp. 727-744, 2003.

[17] J. Shirai, Takashi Yamaguchi, K. Takaba, "Remote Visual Servo Tracking Control of Drone Taking Account of Time Delays, Department Electrical and Electronic Engineering, Ritsumeikan University.

[18] E. Piuzzi, S. Pisa, "Radar cross section measurements of the human body for UWB radar applications," 2012 IEEE International Instrumentation

and Measurement Technology Conference Proceedings, pp. 1290-1293, 2012
[19] B.-K. Park, A. Vergara, O. Boric-Lubecke, V. M. Lubecke and A. Host-Madsen, "Quadrature demodulation with dc cancellation for a Doppler radar motion detector," submitted to IEEE MTT Transactions.
[20] I. Mostafanezhad and O. Boric-Lubecke, "An RF based analog linear demodulator," Proc. IEEE Microw. Wireless Compon. Lett., vol. 21, no. 7, pp. 392–394, Jul. 2011.
[21] C. Gu and C. Li, "DC coupled CW radar sensor using fine-tuning adaptive feedback loop," Electron. Lett., vol. 48, pp. 344–345, 2012.

Robert H. Nakata received his Ph.D. in Electrical Engineering at the University of Hawaii at Manoa, M.S.E.E./C.S. and B.S.E.E degrees from the Massachusetts Institute of Technology, Cambridge, MA in 2017, 1985 and 1981, respectively. He also received the M.B.A. degree from the Wharton School of Business, University of Pennsylvania, Philadelphia, in 2004.

He is the former CEO and CTO of Kai Sensors and the founder of Oahu Group LLC, where he was the recipient and Principal Investigator for a Small Business Innovative Research award. He is currently a lecturer at the University of Hawaii and a Visiting Professor at Ritsumeikan University in Japan. Prior to returning to Hawaii, he was a serial entrepreneur and Vice President of Engineering at Silicon Valley startups and public companies.

Dr. Nakata holds two patents with several more pending and is a Distinguished Member of the National Academy of Inventors, University of Hawaii chapter. He was the recipient of the NSF East Asia Pacific Summer Institute post-doctoral award, won the IEEE IMS 2015 Graduate Student Challenge, was the recipient of the 2016 Honolulu Chapter ARCS engineering award and actively participates in the local startup ecosystem in Honolulu.

Victor M. Lubecke received the B.S.E.E. degree from the California Polytechnic Institute, Pomona, in 1986, and the M.S. and Ph.D. degrees in electrical engineering from the California Institute of Technology, Pasadena, in 1990 and 1995, respectively.

Prior to joining the Department of Electrical Engineering, University of Hawaii at Manoa, Honolulu, as an Associate Professor in 2003, he was with Bell Laboratories, Lucent Technologies, where his research focused on sensing and monitoring technologies for biomedical and industrial applications and on microelectromechanical systems (MEMS) and three-dimensional wafer-scale integration technologies for wireless and optical communications.

Dr. Lubecke is a Fellow of the Institute of Electrical and Electronics Engineers (IEEE). He is an emeritus Distinguished Microwave Lecturer (2006–2008) of the IEEE Microwave Theory and Techniques Society (IEEE MTT-S), and a Topic Editor for the IEEE Transactions on Terahertz Science and Technology. He was Vice Chair of the 2017 IEEE International Microwave Symposium held in Honolulu, HI.

.

Brian Haruna was born in Redwood City, California, in 1981. He graduated with his Bachelors Degree in Electrical Engineering at the University of Hawai'i at Mānoa in 2016. Mr. Haruna completed the Naval Nuclear Propulsion Program in 2006 and served aboard the SSN 766 USS Charlotte as a Nuclear Field Electronics Technician from September 2006 to December 2010.

Takashi Yamaguchi graduated with a bachelors degree in Electrical and Electronic Engineering from Ritsumeikan University in April 2017.

He is now pursuing his Masters degree in Electrical Engineering at the Graduate School of Science and Engineering, Ritsumeikan University. Mr. Yamaguchi's research interests include automatic flight control of drones via visual feedback.

Shigeru Takayama received the Dr. degree in Engineering from Ritsumeikan University in 1995. He is a Professor at the College of Science and Engineering, Ritsumeikan University in Japan and lectures in the Department of Electrical and Electronic Engineering.

His research activities are in the field of measurement engineering and hybrid sensing network systems with telemetric measurements.

Dr. Takayama also contributes to the advancement of measurement engineering and development of human resources in the Society of Instrument and Control Engineers (SICE) and the International Measurement Confederation (IMEKO).

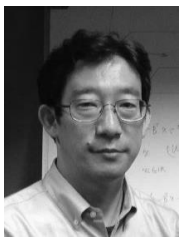

Kiyotsugu Takaba received his M.S., and Dr.Eng. degrees all from Kyoto University, Japan, in 1991, and 1995, respectively. He was an assistant professor and an associate professor at the Department of Applied Mathematics and Physics, Kyoto University, from 1991 to 1998, and from 1998 to 2012, respectively.

In 2012, he joined the Department of Electrical and Electronic Engineering, College of Science and Engineering, Ritsumeikan University, where he is currently a full professor.

Dr. Takaba's current research interests include optimal control, robust control, multi-agent control systems, and their applications. Dr. Takaba is a member of ISCIE, IEEE, and SIAM.